Experimental and Simulation Studies of Heat Transfer in Polymer Melts

Hongbing Chen, Uttandaraman Sundararaj, and K. Nandakumar
Dept. of Chemical and Materials Engineering, University of Alberta, Edmonton, Canada, T6G 2G6

The heat transfer of a single solid cylindrical poly(ether imide) (PEI) pellet in polyethylene (PE) melt under simple shear flow was studied using experiments and numerical simulations. This included two approximate 2-D representations of the geometry, and a rigorous 3-D geometry matching the experimental conditions. A generalized power-law viscosity model for PE melt, and temperature-dependent conductivity and specific heat were used for PEI in the models. Viscous dissipation was included in the simulations. From the experimental temperature history, the mean heat-transfer coefficient $\bar{h}$ was determined to be 370 $W/m^2 \cdot K$, with the assumption of a uniform convective environment. From the simulation, $\bar{h}$ was determined to be 1,160 $W/m^2 \cdot K$ and 420 $W/m^2 \cdot K$ in the 2-D simulations with circular and rectangular pellet, respectively, and 250 $W/m^2 \cdot K$ for the 3-D simulation. Results from the 3-D simulation proved that the uniform convection assumption used to calculate $\bar{h}$ for the experiment was not acceptable.

Introduction

Understanding of heat-transfer-related problems during polymer blending is one of the very fundamental steps to control the polymer blend morphology. In particular, heat transfer between solid polymer pellets and a polymer melt is extremely relevant to modeling polymer blend processing. Numerical modeling is becoming a powerful tool to study the extrusion process, especially considering the ever-increasing power of computers. Thus, the models can incorporate physical-property variations with processing conditions, such as temperature and local shear rates, as well as accommodate complex geometries of the polymer processing equipment. The computational algorithms are becoming sophisticated to be able to handle free surface deformations, such as melting that occurs as a pellet moves down the extruder. Two basic flows are generated inside extruder channels: viz., shear flow and extensional flow. The right combination of these flows is used to achieve good mixing action. Numerous articles reveal the close relationship between polymer blend properties and its morphology (for example, Wu, 1985; Bucknall et al., 1986; Favis and Chalifoux, 1987; Majumdar et al., 1994; Sundararaj et al., 1995; Kudva et al., 1999). The morphology of polymer blends is determined by the individual components' properties as well as processing conditions (for example, Willis et al., 1991; Utracki and Shi, 1992; Sundararaj and Macosko, 1995; Sundararaj, 1996; Huneault et al., 1995; Oshinski et al., 1996; Levitt et al., 1996; Li et al., 1999; Qian and Gogos, 2000).

Experimental studies of the polymer blending process show that significant morphology change occurs during the initial melting of polymers during extrusion (for example, Scott and Macosko, 1991, 1995; Sundararaj et al., 1992; Lindt and Ghosh, 1992; Potente et al., 2001). The detailed information of heat transfer between the barrel and polymer pellets, and between the melted polymer and polymer pellets under actual stress fields are essential to understand the morphology development as well as to design new mixing devices. Heat transfer strongly depends on the flow conditions, such as velocity and pressure. Chandrasekaran and Karwe (1997) measured the velocity profiles of a Newtonian fluid in a reversing section of a corotating twin-screw extender, while Bravo et al. (2000) obtained the pressure and velocity profiles in kneading elements through numerical simulations.

Sastrohartono et al. (1995) and Chiruvella et al. (1996) divided the flow domain in a twin-screw extruder into a translation region and intermeshing region. They also studied the heat transfer and the fluid flow for non-Newtonian polymers

Correspondence concerning this article should be addressed to U. Sundararaj or K. Nandakumar.

using numerical methods. In their study, only one component was included, thus no information about morphology development along the extrusion channel could be obtained from their models. The concept of equivalent radius was adopted by Lai and Yu (2000) to study the heat transfer for blending two polymer phases in a single-screw extruder. In their model, the melting behavior of solid polymer was simplified to that of a metal, which is obviously not true for real polymers. Qian and Gogos (2000) discussed the contributions of deformation of solid pellets to the thermal energy inside an extruder. Tenge and Mewes (2000) focused on the metering zone of a twin-screw extruder and studied the heat balance experimentally. Only one phase was involved; however, viscous dissipation was included in their study. Potente's research group (Potente and Melisch, 1996; Potente and Bastian, 2001; Potente et al., 2001) concentrated on the melting of polymer granules in a twin-screw extruder to study the morphology change during melting. Mean temperature of a solid pellet and a pure drag flow model were used in their theoretical investigation of the melting process. The solution was done analytically using a steady-state approximation to what is inherently a transient heat-transfer process.

In the present work, the heat-transfer characteristics between a single solid polymer pellet and a polymer melt under a predominantly shear flow condition in a batch mixer was studied experimentally. This corresponds to the initial process of a pellet heated in a polymer melt before it softens and deforms. Specifically, the temperature history at the center of an initially cold cylindrical pellet immersed in a melt was monitored. Such a history was used to back calculate a heat-transfer coefficient between the pellet and the melt. The same process was modeled using the standard continuum mechanical equations and the generalized non-Newtonian model. Important variations of thermal properties with temperature were also accounted for using measured values of such properties. The equations were solved using the standard finite-element tools that are available in the package FIDAP (Fluent Inc.). A heat-transfer coefficient was also calculated from the simulation results.

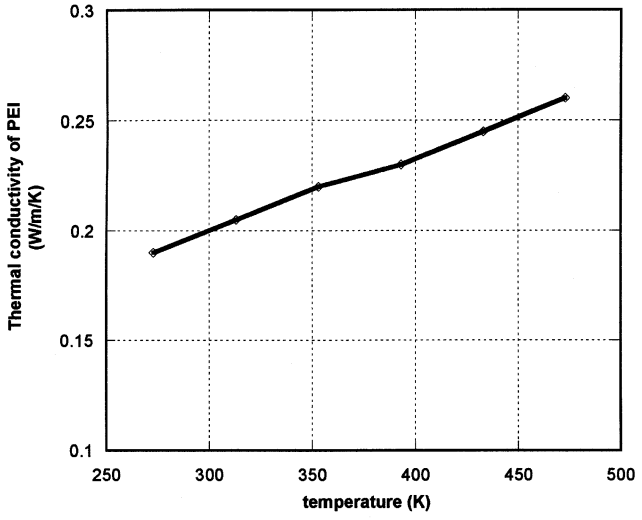

Figure 1. Variation of thermal conductivity with temperature for PEI. (Data supplied by GE Plastics.)

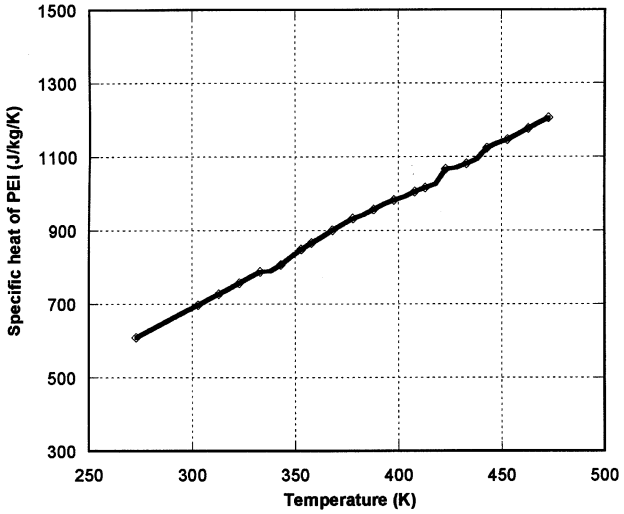

Figure 2. Specific heat of PEI with temperature.

Experimental Procedures

Polymer properties

Two polymers were used in the present work: viz., polyetherimide (PEI) from GE Plastics and polyethylene (PE) from Petromont, Canada. PE was the matrix phase, and PEI was the dispersed phase in the form of a pellet. PEI has a much higher softening temperature than PE, so that the PEI pellet was in the solid state during the entire process. Figure 1 shows the thermal conductivity of PEI as a function of temperature.

The specific heat of the two polymers was measured using a TA Instruments DSC 2910, and Thermal Analyst 2200 software was used to analyze the data. The heating rate was 20°C/min. Figure 2 shows the specific heat variation of PEI with temperature. For the matrix PE, a constant thermal conductivity $k_{PE} = 0.182$ W/m·K was used since its temperature had small variation during the whole process (Han et al., 1990). Its specific heat variation with temperature is shown in Figure 3. Since polymers melt over a range of temperatures,

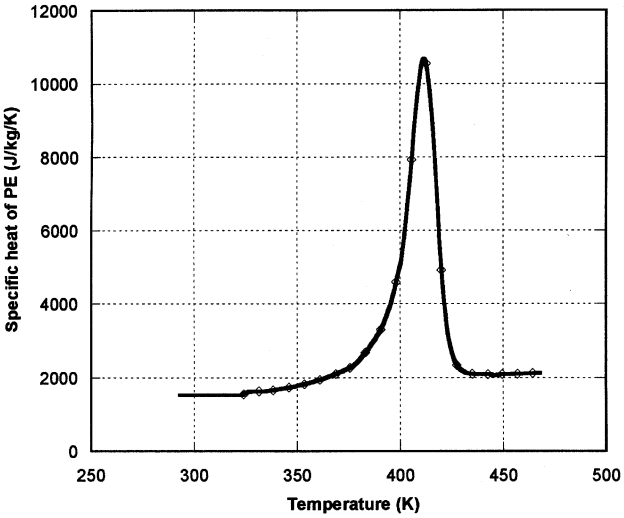

Figure 3. Specific heat of PE with temperature.

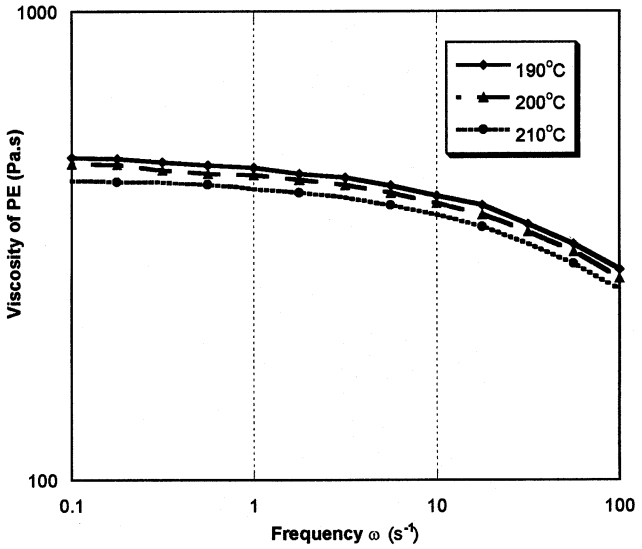

Figure 4. Viscosity of PE at three different temperatures.

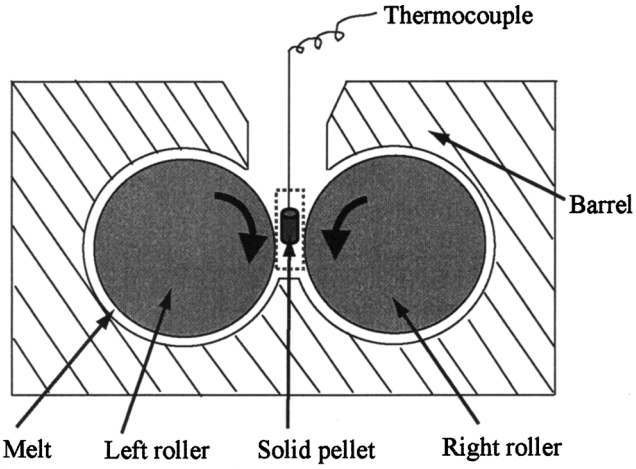

Figure 5. Batch-mixer experimental setup.

not at one specific temperature, we approximated the enthalpy change due to melting using specific heat data (that is, the specific heat peak in Figure 3 can be integrated over temperature to obtain the enthalpy change due to fusion).

The dynamic rheological properties of PE were determined using a Rheometrics RMS 800 rheometer with parallel-plate fixtures. Figure 4 shows the variation of shear viscosity of PE with frequency at different temperatures. Using the Cox–Merz rule, which states that the complex viscosity vs. frequency curve is almost exactly like the steady shear viscosity vs. shear-rate curve, we were able to use the dynamic data in our model. A consistent shear-thinning behavior is observed at different temperatures. A correlation proposed by Van Krevelen et al. (1976) is used to generate the functional form of the temperature-dependent viscosity of PE. Based on the shear thinning and temperature effects, a generalized power-law viscosity model was obtained as

$$\eta = 350 \times 470 \times \dot{\gamma}^{(n-1)} \times \exp(-0.02 \cdot T + 1.88 \times 10^{-5} T^2), \quad (1)$$

where the power exponent $n = 0.9$. At lower shear rates, the viscosity was only dependent on temperature and the power-law constant was set to 1.0.

Batch-mixer experiment

The Haake Rheocord 90 Torque Rheometer fitted with a series 600 internal batch mixer was used for the experiments. Two cylindrical rollers were built to generate a simple flow in the mixer. Figure 5 shows the experiment setup. Since we replaced the normal rollers, which have indents with cylindrical rollers, the melt volume was significantly reduced by using the cylindrical rollers. All materials were heated at 80°C under vacuum for 12 h before being added into the mixer. The barrel temperature of the mixer was preheated to 190°C, and the motor speed was set at 50 rpm. About 16 g PE was added to the mixer to form the melt phase. To record the temperature history of the pellet, a small hole was drilled along the cylinder axis of the PEI pellet, but not through the full length of the pellet. The size of the hole was carefully controlled so that a thermocouple could be inserted into the hole, and the thermocouple was in close contact with the inner surface of the hole in the pellet. Epoxy was used to glue the thermocouple with the pellet so that there was no air between the surfaces to create any thermal contact resistance. The thermal conductivity ($k = 0.20$ W/m·K) of the epoxy was comparable to the solid PEI pellet. Before the PEI pellet was inserted into the PE melt, the PE melt temperature was measured, and its value was set as the reference temperature for the corresponding simulations. For our experiment, the reference temperature was measured to be 197°C. The temperature history of the central point was recorded at every 0.1 s using an OPTO 22 data-acquisition system.

The classic analytical solution for transient conduction heat transfer from a cylindrical pellet to an infinite medium subject to a convective boundary condition was used to determine the mean heat-transfer coefficient on the melt side by matching the experimentally measured temperature history at the center of the pellet with the analytical model. This method involves using the superposition of transient solutions that is well documented in standard heat-transfer textbooks (for example, Incropera and DeWitt, 1996). Table 1 summarizes all the parameters that are used in the calculation. Figure 6 shows the flow diagram to calculate the mean $\bar{h}$-value from experimental data (refer to Incropera and DeWitt (1996) for transient infinite cylinder and infinite plane wall equations). This model, of course, assumes that all the

Table 1. Parameters of PEI Pellet Used in Calculating the Mean h-Value from Experimental Data

Parameter	Value
ρ (kg/m^3)	1,270
C_p (J/kg·K)	938
k (W/m·K)	0.23
T_{ref} (K)	470
D (mm)	2.0
L (mm)	12

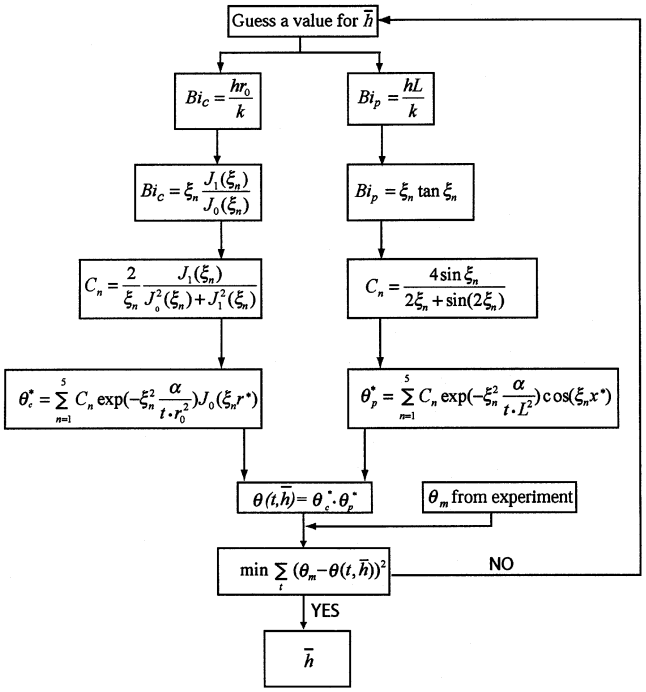

Figure 6. Flow diagram for calculating the mean heat-transfer coefficient, $\bar{h}$, from the experimental temperature history.

cylindrical surfaces are exposed to the same heat-transfer environment at all times, hence what we calculate as a heat-transfer coefficient from this approach can be thought of as an effective mean heat-transfer coefficient from the pellet on the melt side. In particular it is to be treated as an average over the interface and over the time interval. We can only obtain this effective mean heat-transfer coefficient from the single temperature measurement made in the experiment. In the actual experiments, since there is an unsymmetrical flow around the pellet, and the viscosity is a function of temperature, the heat-transfer environment around the pellet–melt interface will not be uniform in space and time and the heat-transfer coefficient changes with space and time. Such variation will be taken into account in the simulations.

Model Equations

The governing equations are the standard conservation laws for mass, momentum, and energy. The following assumptions were made to model the flow around the pellet that is placed in the gap between two cylindrical rollers. The melt is assumed to be incompressible and inelastic, but its viscosity obeys the generalized power law. Viscous dissipation is included in the energy equation for the melt phase. The polymer melt is assumed to be in perfect contact with the pellet, and, hence, the contact resistance between the melt and the pellet is assumed to be zero. For the PE melt, the governing equations are as follows

Continuity Equation

$$\nabla \cdot V = 0. \tag{2}$$

Momentum Equation

$$\rho\left(\frac{\partial V}{\partial t} + V \cdot \nabla V\right) = -\nabla P + \nabla \cdot \bar{\bar{\tau}}, \tag{3}$$

where the shear stress τ is related to the rate of strain tensor D, through

$$\bar{\bar{\tau}} = 2\eta(\dot{\gamma}, T)\bar{\bar{D}}, \tag{3a}$$

and η is the non-Newtonian viscosity, which has the following form

$$\eta = \eta_0 m e^{(-aT+bT^2)} \dot{\gamma}^{(n-1)}. \tag{3b}$$

Energy Equation

$$\rho C_p\left(\frac{\partial T}{\partial t} + V \cdot \nabla T\right) = \nabla \cdot (k \nabla T) + \bar{\bar{\tau}} : \nabla V. \tag{4}$$

The energy equation was used for the PE melt. Because the velocity inside the pellet is zero and there is no viscous dissipation, for the PEI pellet, the energy equation is reduced to the following transient heat-conduction equation:

$$\rho C_p \frac{\partial T}{\partial t} = \nabla \cdot (k \nabla T). \tag{5}$$

Boundary conditions

Two 2-D models were built to simulate the flow in the gap between the two cylinders of the batch mixer. To capture the flow characteristics of the experiment, there are two possible orientations for the pellet in the simulations. If we assume the axis of the cylinder is in the z-direction perpendicular to the paper and infinitely long in that direction, the pellet can then be orientated either as a circle perpendicular to the axis of the cylinder or as a rectangle parallel to the axis of the cylinder. The geometry and boundary conditions are shown in Figures 7a and 7b. All the material properties used in the simulations are summarized in Table 2. Obviously, there are important geometrical differences between the experiments and the 2-D simulations. To eliminate the geometry difference, a 3-D batch-mixer geometry was built and is shown in Figure 7c. The 3-D geometry is the same as the experimental setup except for the length of the cylinders, which was reduced from 47 mm to 6 mm to save computational cost. Even so, the time required for the 3-D simulation was about 10 times longer than the time required for the 2-D cases. Therefore, if the 2-D representations are accurate, it would be advantageous to use them in future modeling efforts. The finite-element grid distributions are shown in Figures 8a–8c for the three geometrical variations.

The 2-D geometries are treated as open systems with inflow and outflow boundaries, while the 3-D geometry is a closed system with all of the polymer melt inside the batch mixer. A no-slip condition is imposed at all of the wall boundaries. For the 2-D case, at the left and right boundaries, the vertical component of the velocity is set to zero, but the horizontal component is computed by the Galerkin

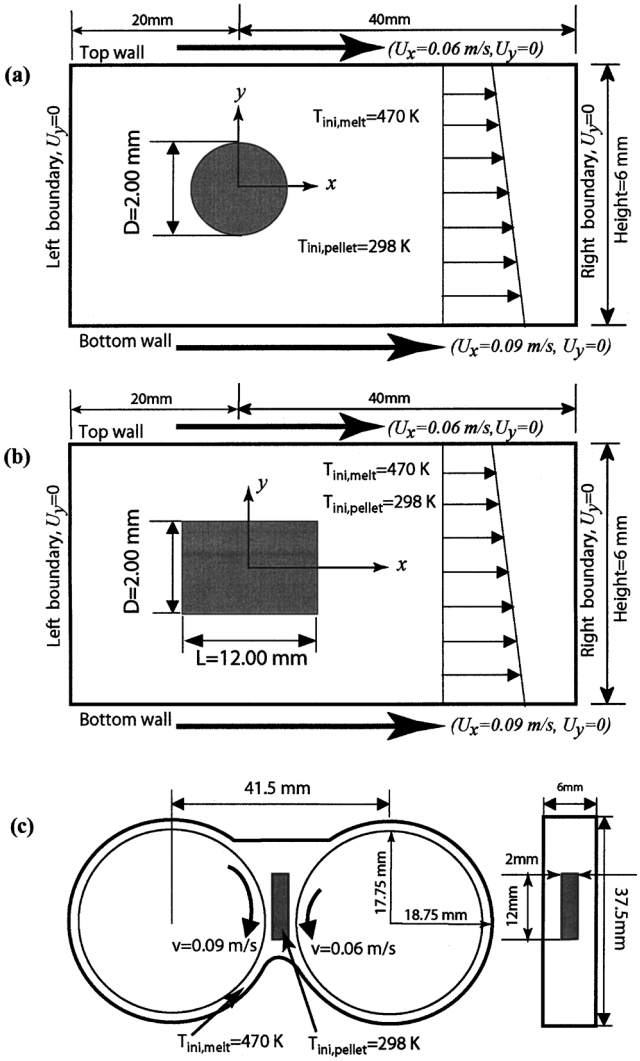

Figure 7. Geometric model and boundary conditions: (a) 2-D approximation with axis perpendicular to flow; (b) 2-D approximation with axis parallel to flow; (c) 3-D geometry of the batch mixer.

Figures not to scale.

finite-element method (FEM). For the temperature, an isothermal condition is imposed on the walls, with the temperature being equal to the initial melt temperature, while the interface between the melt and the pellet have the same temperature on the melt and pellet side of the interface. The heat flux across the interface is also imposed to be continuous. For the velocities, the no-slip condition is also imposed at the pellet–melt interface. Note that the two rollers in the experiments rotate at different speeds; the right roller rotates

Table 2. Property Values of PE and PEI Used in the Simulations

Sample	ρ (kg/m^3)	C_p (J/kg·K)	k (W/m·K)	η (Pa·s)
PE	954	Figure 3	0.182	Eq. 1
PEI	1,270	Figure 2	Figure 1	Solid

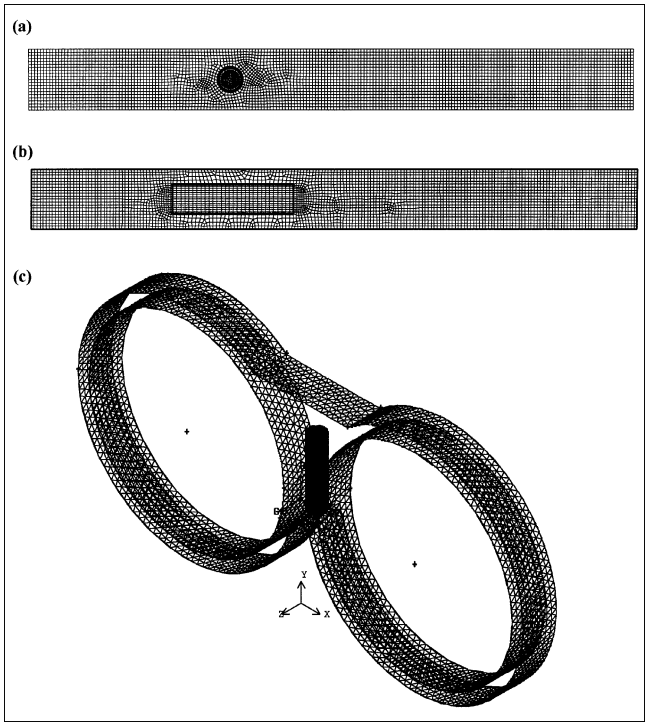

Figure 8. Finite-element grid distribution for the three geometries considered in this work.

at two-thirds the speed of the left roller. Hence the upper and lower plate velocities in the case of 2-D simulations are set at 0.06 and 0.09 m/s, respectively, and, of course, the 3-D simulation uses the different speeds for the two rollers.

The successive substitution (S.S.) method was used to solve the nonlinear system of equations at each time step using the solver FIDAP version 8.6. The time integration was performed using the backward Euler method. Once the solution is obtained, macroscopic quantities like average temperature or heat-transfer coefficients can be computed at each instant of time. The local heat-transfer coefficient at every point on the interface is calculated from the equation

$$h_i = \frac{q_i''}{T_{\text{ref}} - T_i}, \tag{6}$$

where q_i'' is the local heat flux at a point on the interface that is computed from Fourier's law applied on the pellet side using, $q'' = -k\nabla T$, T_{ref} is the reference temperature, which is 470 K for this work, and T_i is the local interface temperature. The local heat-transfer coefficient can then be integrated over the interface A_i to get an average heat-transfer coefficient at each instant of time from

$$\bar{h}(t) = \frac{\int h_i \, dA_i}{A_i}. \tag{7}$$

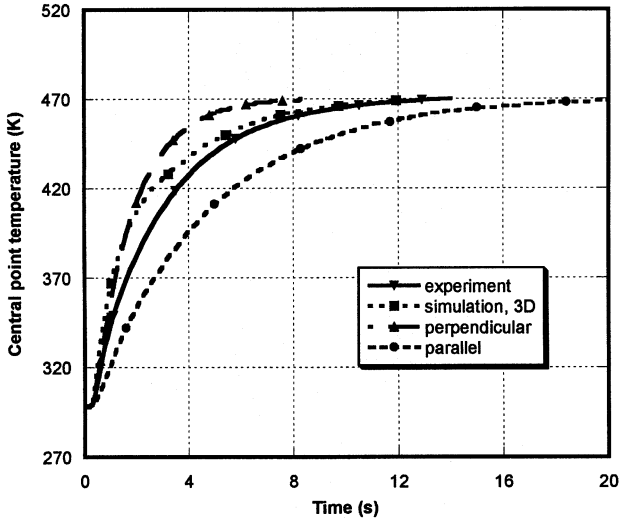

Figure 9. Comparison of the experimentally measured center-point temperature with those predicted from the simulations.

Thermocouple dynamics were not accounted for.

The time-average heat-transfer coefficient $\bar{h}$ is found using

$$\bar{h} = \frac{\sum_{n=1}^{N} \bar{h}(t)}{N\Delta t}, \tag{8}$$

where Δt is the time step and N is the number of time steps.

Results and Discussion

Experimental results

Figure 9 shows the pellet's inner temperature vs. time for the experiment and the three different simulations. The time for the pellet to reach the reference temperature from 3-D simulation matches well with the time from the experiment, although there are important differences in the temperature history that require further scrutiny, namely, the rates of temperature increase in the simulations were not the same as that in the experiment, even for the 3-D simulation. This is attributed to the dynamics of the thermocouple.

Every type of thermocouple has its own characteristic dynamics. A first-order time constant is widely used to capture this. To measure the time constant of the thermocouple, we used the OPTO 22 data-acquisition system to record its temperature history after inserting the thermocouple into an oil bath held at a certain temperature. The time when the recorded temperature reached 63% of the final temperature was taken to be the thermocouple's time constant for the measuring temperature. An average time constant was calculated based on time constants obtained with different bath temperatures. According to our measurement, we found that the time constant of the thermocouple used in the experiment is about 0.9 s. This value is very close to the time constant of 1.0 s supplied by the thermocouple manufacturer (Omega Engineering, Inc.).

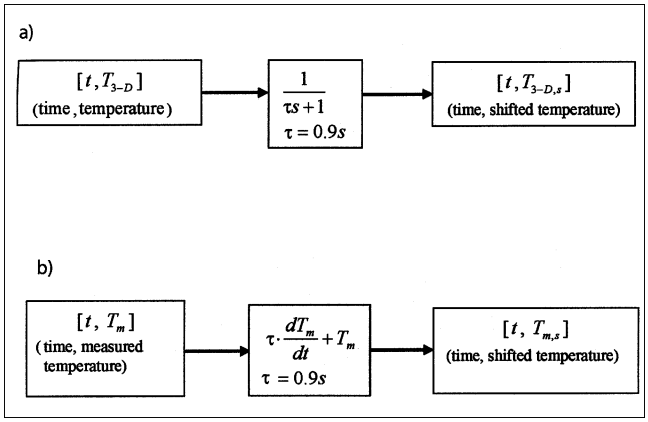

Figure 10. First-order process approximation of the thermocouple dynamics (time constant = 0.9 s): (a) model used to shift the 3-D simulation curve to include thermocouple delay; (b) model used to shift the experimental curve to remove thermocouple delay.

The first-order process approximation of the thermocouple was employed to shift the data from the 3-D simulation to include the thermocouple dynamics, and to shift the data from experiment to remove the thermocouple dynamics to see how well the two sets of data matched. Figure 10 shows the block diagrams of the two process approximations. The thermocouple dynamics were added to the simulation result, and the shifted curve is shown in Figure 11a. The measured experimental curve is also shown for comparison. It can be seen that the shifted simulation curve and the measured data match quite well. The thermocouple dynamics were removed from the experimental data, and the shifted curve is shown in Figure 11b. Again, we see that simulation and experiment match well if we account for the thermocouple dynamics.

In the initial stages, since temperature was differentiated with time to shift the measured experimental data, a small variation in the recorded temperature could cause large oscillations, as seen in Figure 11b. The discrepancy at the initial stage may also be due to the heat transferred into the polymer pellet through the thermocouple itself, which would cause the central temperature to rise faster in the experiment than in the simulation, while at later stages, heat was taken out from the pellet because the temperature of the thermocouple was higher than the air outside the batch mixer. This may explain why the temperature rise in the experiment is slower than that seen in the shifted simulation curve (see Figure 11a).

Based on the uncorrected experimental temperature history and using the algorithm outlined in Figure 6, the mean h-value from the experiment was computed to be $\bar{h} = 370$ W/m$^2\cdot$K. This $\bar{h}$-value was obtained based on the assumption of uniform convective environment, and the thermocouple's dynamics were not accounted for. To shift the experimental curve to account for the thermocouple dynamics, we needed to take a derivative of the measured temperature (see Figure 10b), which created error and oscillations as shown in Figure 11b. Therefore, we used the uncorrected data for the initial determination of the $\bar{h}$-value. Figure 12 shows the comparison between the curve from experiment and the one

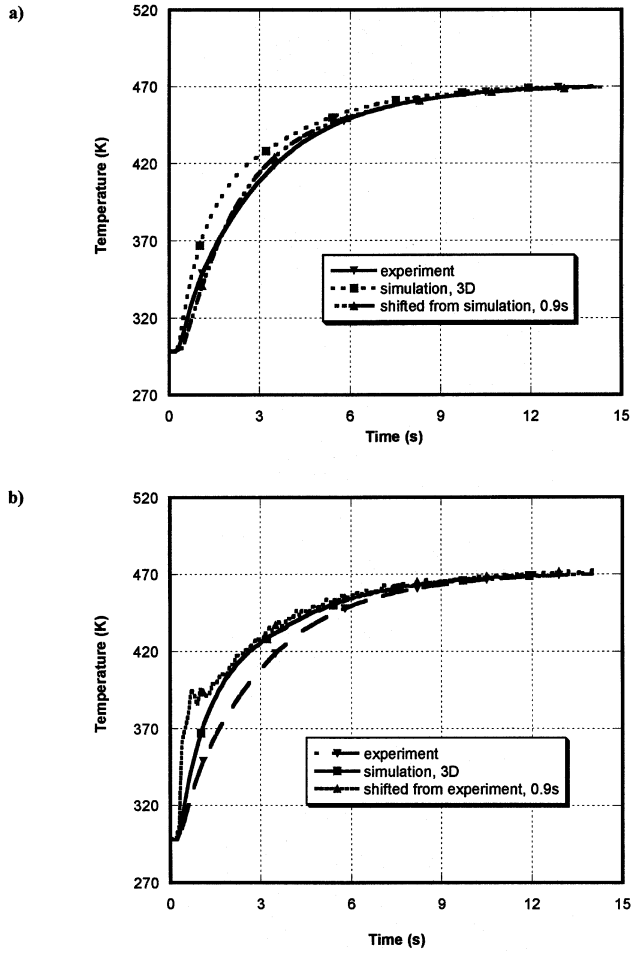

Figure 11. Results of shifting 3-D simulation and experiment data using a first-order process approximation with time constant 0.9 s: (a) simulation curve shifted to include thermocouple delay; (b) experimental curve shifted to remove thermocouple delay.

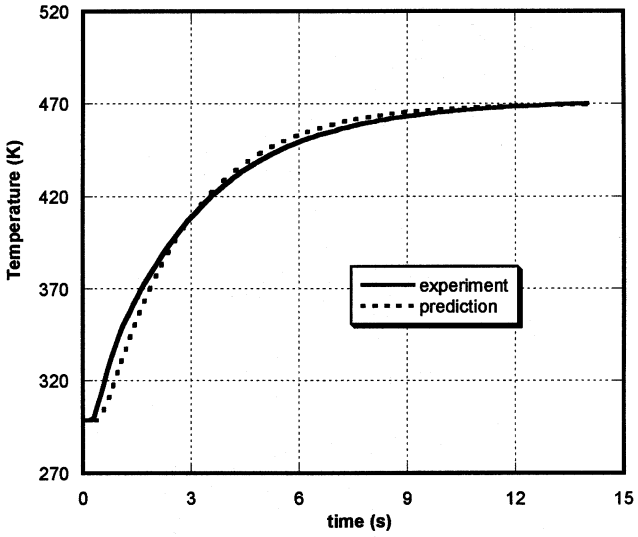

Figure 12. Comparison of the center-point temperature curves from the experiment and that predicted with $h = 370$ W/m$^2\cdot$K using algorithm outlined in Figure 6.

predicted using a constant value of $\bar{h} = 370$ W/m$^2\cdot$K. It is seen that the predicted temperature rises slower than the experimental one initially, and at later times, the slope of the predicted curve is larger than the experimental one. The discrepancy between the two curves may be due to the assumptions we made. While the same algorithm (Figure 6) can and will be used to determine an average heat-transfer coefficient from each of the simulations, such a calculation would be subject to the same assumptions as uniform convective environment, which is a necessary assumption in the case of experimental data, but an unnecessary one in the case of simulation, as local and average heat-transfer coefficient can be calculated according to Eqs. 6 and 7.

Figures 13a–13c present heat-transfer coefficients obtained from Eqs. 6 and 7 vs. different times from the 2-D and 3-D batch-mixer simulations. Since the heat flux at the interface has a singularity (infinite heat flux) at $t = 0$, there are large numerical errors at the beginning of the simulation. Similarly, at the end of the simulation, temperatures at some nodes along the interface are almost equal to the reference temperature, leading to division by zero in the heat-transfer coefficient calculation, and thus resulting in large errors. Hence the results for heat-transfer coefficients are presented for a certain time range. Using Eqs. 6–8, the average heat-transfer coefficients for each of the three cases were determined to be 1,160, 420 and 250 W/m$^2\cdot$K for the 2-D circle, 2-D rectangle, and 3-D cylinder, respectively. Table 3 summarizes all the calculated heat-transfer coefficients and the time ranges used to calculate them.

Heat transfer for an infinite-length circular cylinder in crossflow is correlated by the Churchill equation (Churchill and Bernstein, 1977)

$$\overline{Nu}_D = 0.3 + \frac{0.62\,Re_D^{1/2}Pr^{1/3}}{\left[1+(0.4/Pr)^{2/3}\right]^{1/4}}\left[1+\left(\frac{Re_D}{282{,}000}\right)^{5/8}\right]^{4/5}, \quad (9)$$

where the Reynolds number is $Re_D = 0.00039$ and the Prandtl number is $Pr = 4.3\times10^6$ for this work. From this correlation, the mean heat-transfer coefficient was calculated to be 210 W/m$^2\cdot$K. Although the flow condition is different from our experiment, the value is surprisingly close to the one found from the simulation results. Rao (2000) provided another correlation for non-Newtonian flows over a cylinder in crossflow. Using this correlation, the calculated heat-transfer coefficient is over 2,000 W/m$^2\cdot$K; however, the Re number and Pr number in our work are not within the ranges specified for use of this correlation.

Based on the shifted experimental curve shown in Figure 11b, using the algorithm outlined in Figure 6, the mean heat-transfer coefficient, $\bar{h}$, was calculated to be between 600 and 650 W/m$^2\cdot$K. This value is much larger than the value obtained by averaging the local heat-transfer coefficients from the 3-D simulations (250 W/m$^2\cdot$K). For comparison, the same algorithm (shown in Figure 6) was used to calculate $\bar{h}$ based

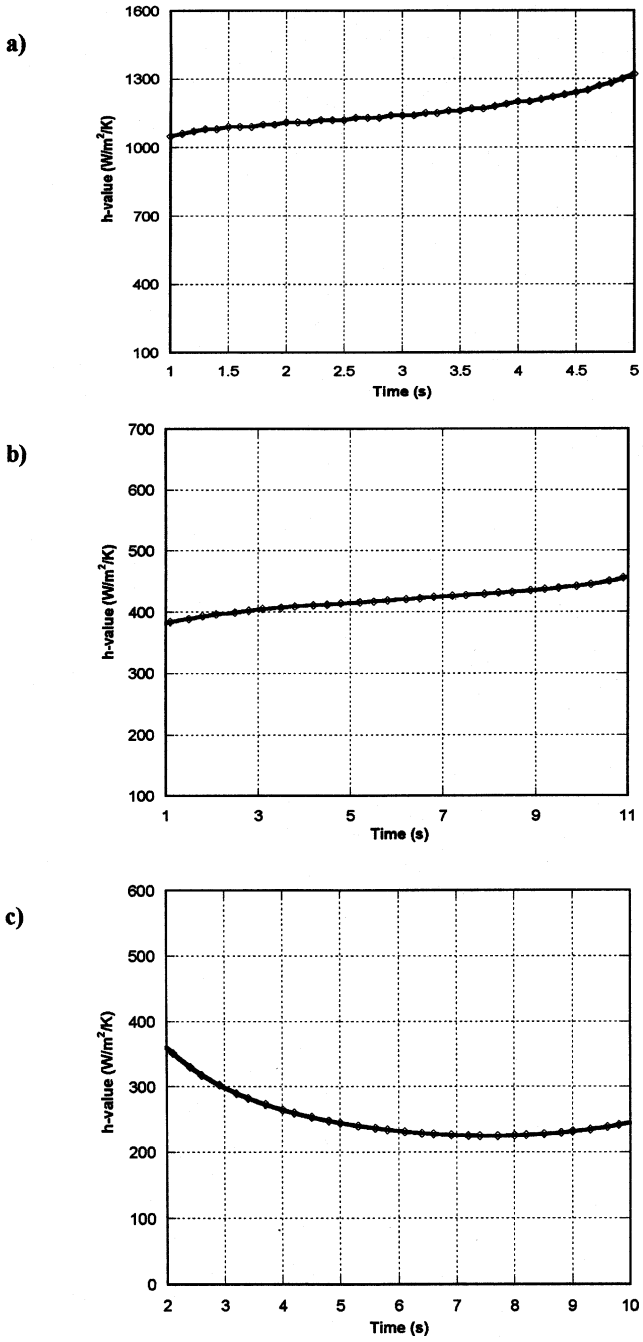

Figure 13. Variation of spatially averaged h-values with time: (a) 2-D simulation with axis perpendicular to the flow ($h = 1{,}160$ W/m$^2\cdot$K); (b) 2-D simulation with axis parallel to the flow ($h = 420$ W/m$^2\cdot$K); (c) 3-D simulation ($h = 250$ W/m$^2\cdot$K).

on the center-point temperature data from the 3-D simulation; however, the calculated value for $\bar{h}$ was also over 600 W/m$^2\cdot$K, which is not consistent with the value calculated using the heat-flux and temperature data from the simulation (250 W/m$^2\cdot$K). Therefore, the assumption of an even convective environment used in the algorithm outlined in Figure 6 is not an acceptable one to calculate $\bar{h}$. If we consider real

Table 3. Heat-Transfer Coefficients from Experiment and Simulations

Data Source and Method	$\bar{h}$ (W/m$^2\cdot$K)	Time (s)
2-D simulation-circle*	1,160	1 ~ 5
2-D simulation-rectangle*	420	1 ~ 11
3-D simulation-cylinder*	250	2 ~ 10
Data from 3-D simulation-cylinder**	>600	0 ~ 14
Measured data from exp.**	370	0 ~ 14
Data removing time delay from exp.**	>600	0 ~ 14
Churchill correlation	210	

*Integration from local heat-transfer coefficient—Eqs. 6–8.
**Algorithm outlined in Figure 6.

polymer pellets used in polymer processing, which are short cylinders with L/D of about one, the assumption of uniform convective environment is even less valid.

We can see the match between the simulation and the experiment by comparing the center-point temperature curves obtained from the 3-D simulation and the experiment. From Figure 11, we see that the simulation and experimental temperature vs. time curves match well if we account for the thermocouple dynamics. Therefore, we can assert that the heat-transfer coefficient obtained from simulation is the correct heat-transfer coefficient, since it accounts for the uneven convective environment.

Comparison between the experiment and the simulations shows that the 3-D simulation represents the experimental process the best. From the simulation, we can get a more accurate value for the heat-transfer coefficient than that from the experiment, because no assumption for even convective environment and no effect of thermocouple dynamics were included in the calculation of the heat-transfer coefficient value for the 3-D simulation.

Simulation results

One major advantage of the numerical modeling is that detailed information can be extracted from the simulation result. Figure 14 shows the temperature contour and the velocity vectors at a time of 1 s. The velocity has reached its fully developed state already, and dynamic changes in flow due to changes in viscosity near the pellet are small. The effects of heat conduction inside the pellet and heat convection outside the pellet are clearly seen in this figure as shaded contours. The heat transfer inside the pellet is seen to have progressed to a significant level even after 1 s. In the 2-D simulations, because the velocity of the bottom surface (left roller) is greater than that of the top surface (right roller), a degree of unevenness in the cold region is seen near the faster moving surface.

To obtain detailed quantitative results from the 3-D simulation, variation of field quantities along a line parallel to the x-axis through ($y = 0.0$, $z = -3.0$), which crosses the pellet at the location of the thermocouple, was chosen (Figure 8c shows the x, y, z directions). Figures 15a and 15b show, respectively, the U_y variation and the temperature variation along the chosen line at three different times of 1, 5, and 10 s. The vertical component of the velocity, shown in Figure 15a, shows that the velocity varies linearly in the gap, except near the

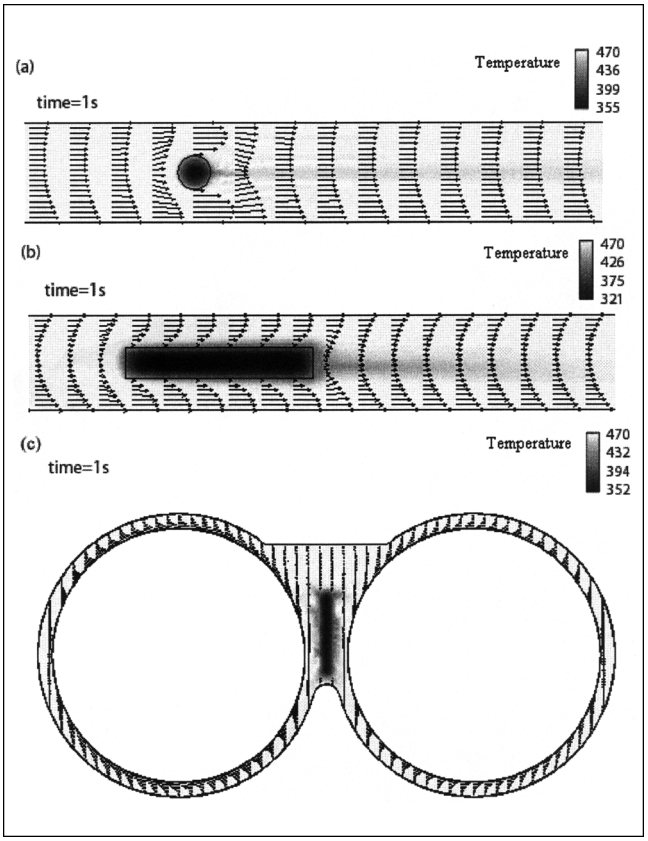

Figure 14. Temperature profile and vector plots of the velocity field for the three cases are shown at the end of 1 s.

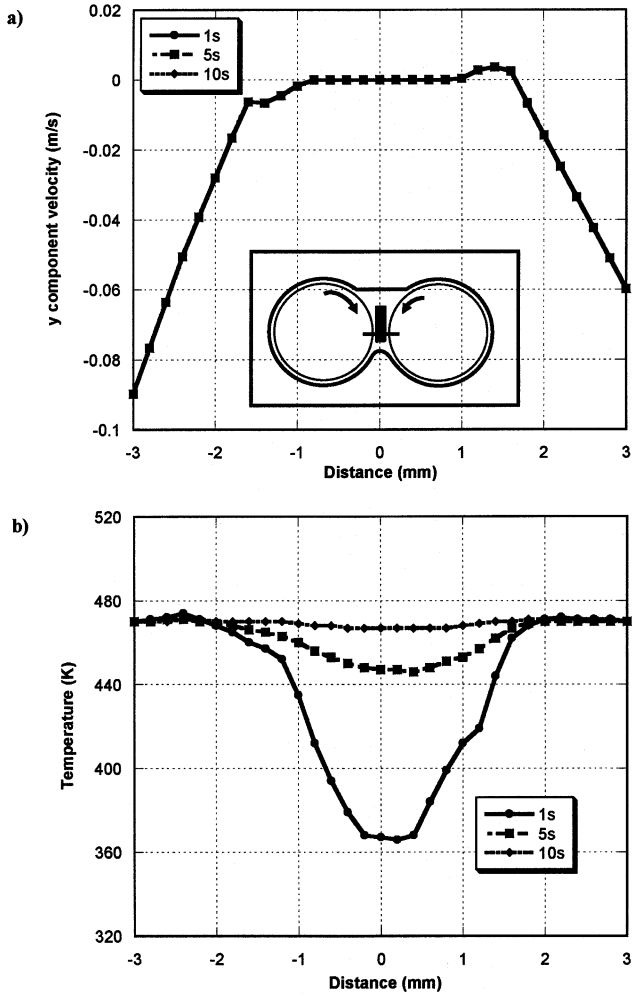

Figure 15. (a) y-Component velocity variation, and (b) temperature variation from the 3-D simulation along x ($y = 0$, $z = -3$).

The sampling line cuts across the pellet as shown in the inset. Axes are defined in Figure 8c.

pellet surface due to temperature-dependent viscosity effects, and it is identical at all three sampling times. From detailed examination of the velocity profiles near the pellet, we saw that there were eddies near the surface of the pellet. For example, the y-component velocity near the right roller at the sampling line is going up or is positive (see Figure 15a) and the melt recirculates down at a higher z-position. It can be seen in Figure 15b that the temperature at the core of the pellet has already changed at 1 s from its initial value of 298 K to over 350 K. At $t = 5$ s and 10 s, the temperature near the left roller (which moves faster) is slightly higher than near the right roller. Actually, the maximum temperatures at $t = 5$ s and 10 s are several degrees higher than 470 K. This is due to a higher rate of viscous heating near the pellet surface, which experiences a higher shear rate. As expected, the rate of temperature change between 5 and 10 s is smaller as the temperature driving force decreases with time.

For a non-Newtonian fluid, like the PE melt in this work, shear rate is another important parameter that affects the flow, and hence the heat transfer. Figure 16 shows the shear rate along the same line across the pellet at three sampling times. Within the solid pellet, the shear rate is always zero. At the interface, the shear rate reaches its maximum value. The different velocities of the left and right roller result in the unsymmetrical shear-rate profiles. There is almost no difference between the profiles at the three times. This result again conforms to the expectation that the shear rate is higher near the left roller and that the flow changes very little with time.

As previously mentioned, the viscosity of PE depends on temperature and shear rate. Figure 17 gives the viscosity variation at different times along the same line through the pellet. There is no viscosity for the solid PEI pellet (distance: -1 mm to 1 mm). From Figure 16, we see that the shear rate is higher at the interface and that it is highest on the lefthand side (where the roller is moving faster). Since polymer melts are shear thinning, high shear rate corresponds to low viscosity, and low shear rate corresponds to high viscosity. Hence the viscosity should be lower at the interface and it should be lowest near the left side, as seen in Figure 17. Furthermore, the effect of temperature on the viscosity can be seen. The initially cool pellet reduces the temperature of the surrounding melt at early times, and hence, the viscosity at $t = 1$ s is higher than at subsequent times. For any time greater than 10 s, there is little temperature variation, so only shear rate affects the viscosity. Even at $t = 1$ s, the sharply increased shear rate very close to the interface dominates the changes

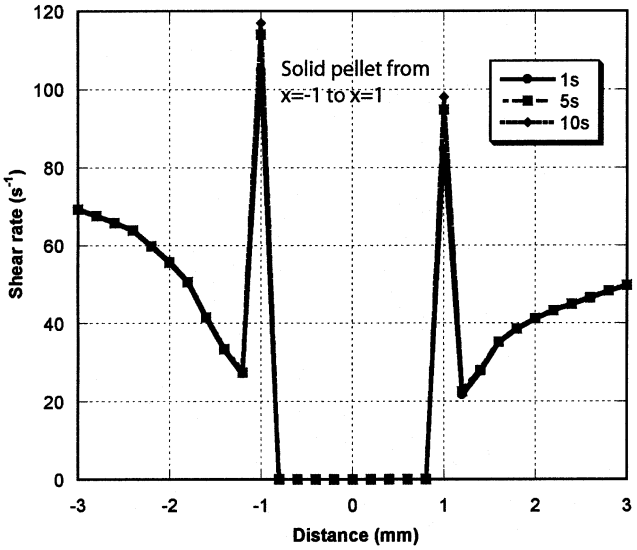

Figure 16. Shear rate plots along a line through the pellet from the 3-D simulation at different times.

The location is along x ($y = 0$, $z = -3$). Axes are defined in Figure 8c.

in viscosity and the viscosity decreases resulting in the steeper velocity gradient near the interface seen in Figure 15a. Obviously, compared to an experiment, much more detailed information about the process can be extracted from the numerical modeling results.

Conclusions

The heat-transfer coefficient was determined experimentally and numerically for a polymer pellet in an intensive mixing flow. The 3-D simulation represents the experiment the best. In the experiment, the dynamics of the thermocouple had a significant influence on the temperature history of the pellet. There was some discrepancy between the temperature curves from the experiment and the 3-D simulation, but by adjusting the data using the thermocouple dynamics, the two temperature curves matched very well. The time for the pellet to reach the reference temperature and the center-point temperature history obtained from the experiment match well with values obtained from the 3-D simulation. Simulation results allowed us to understand the experiment better, and we were able to obtain a more representative heat-transfer coefficient, since we could account for the uneven convective environment in the mixer. It was shown that shear rate and viscosity varied significantly near the pellet surface.

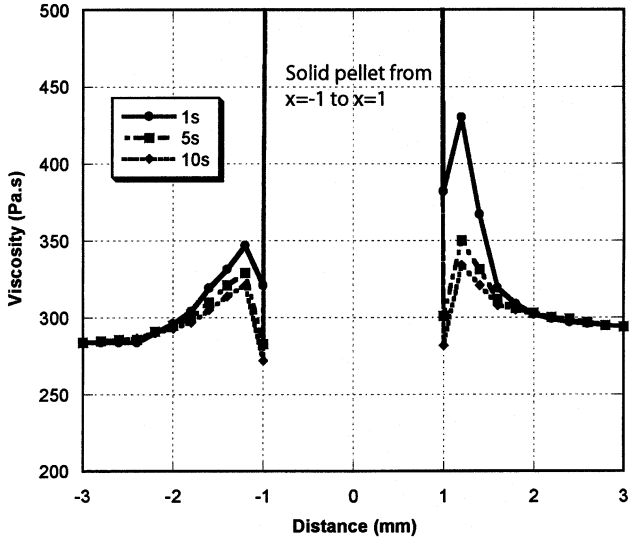

Figure 17. Viscosity plots along a line through the pellet from the 3-D simulation at different times.

The location is along x ($y = 0$, $z = -3$). Axes are defined in Figure 8c.

Acknowledgments

The authors would like to thank Mr. A. Afacan and Mr. W. Boddez for their help in setting up the experiment, and the Natural Sciences and Engineering Research Council of Canada for supporting this research. Portions of this article were presented at CSChE Conference, Halifax, Canada, in October 2001.

Notation

a = constant
A_i = local area
b = constant
Bi_c, Bi_p = Biot number for infinite cylinder and plane wall
C_n = coefficient
C_p = specific heat
D = diameter of the pellet
$\bar{\bar{D}}$ = strain rate tensor
h = heat-transfer coefficient
h_i = local heat-transfer coefficient
$\bar{h}$ = time-averaged mean heat-transfer coefficient
$\bar{h}(t)$ = mean heat-transfer coefficient at time t
J_0, J_1 = Bessel functions of the first kind
k = thermal conductivity
L = length of the pellet
m = constant
$\overline{Nu}_D$ = mean Nusselt number
Pr_D = Prandtl number
q_i'' = local heat flux
Re_D = Reynolds number
s = Laplace transform variable
t = time
Δt = time interval
$T_{3\text{-}D}$ = temperature from 3-D simulation
$T_{3\text{-}D,s}$ = shifted temperature from 3-D simulation
T_i = local temperature
T_m = measured temperature
$T_{m,s}$ = shifted temperature from measurement
T_{ref} = reference temperature
U_x = x-component velocity
U_y = y-component velocity
$\vec{V}$ = velocity vector

Greek letters

α = thermal diffusivity
$\dot{\gamma}$ = shear rate
θ = dimensionless temperature from finite cylinder
θ_c^*, θ_p^* = dimensionless temperature from infinite cylinder and plane wall
θ_m = dimensionless temperature from experiment
η = viscosity
η_0 = zero shear-rate viscosity
ξ_n = roots of transcendental equation
ρ = density
τ = time constant for thermocouple
$\bar{\bar{\tau}}$ = stress tensor
ω = frequency

Literature Cited

Bravo, V. L., A. N. Hrymak, and J. D. Wright, "Numerical Simulation of Pressure and Velocity Profiles in Kneading Elements of a Co-Rotating Twin-Screw Extruder," *Poly. Eng. Sci.*, **40**, 525 (2000).

Bucknall, C. B., F. F. P. Cote, and I. K. Partridge, "Rubber Toughening of Plastics 9: Effects of Rubber Particle Volume Fraction on Deformation and Fracture in HIPS," *J. Mater. Sci.*, **21**, 301 (1986).

Chandrasekaran, M., and M. V. Karwe, "Measurement of Velocity Profiles in Reverse-Screw Elements of a Twin-Screw Extruder," *AIChE J.*, **43**, 2424 (1997).

Chiruvella, R. V., Y. Jaluria, M. V. Karwe, and V. Sernas, "Transport in a Twin-Screw Extruder for the Processing of Polymers," *Poly. Eng. Sci.*, **36**, 1531 (1996).

Churchill, S. W., and M. Bernstein, "Correlating Equation for Forced Convection from Gases and Liquids to a Circular Cylinder in Cross Flow," *J. Heat Transfer*, **99**, 300 (1977).

Favis, B. D., and J. P. Chalifoux, "The Effect of Viscosity Ratio on the Morphology of Polypropylene Polycarbonate Blends During Processing," *Poly. Eng. Sci.*, **27**, 1591 (1987).

Han, C. D., K. Y. Lee, and N. C. Wheeler, "An Experimental Study on Plasticating Single-Screw Extrusion," *Poly. Eng. Sci.*, **30**, 1557 (1990).

Huneault, M. A., Z. H. Shi, and L. A. Utracki, "Development of Polymer Blend Morphology During Compounding in a Twin-Screw Extruder 4: A New Computational Model with Coalescence," *Poly. Eng. Sci.*, **35**, 115 (1995).

Incropera, F. P., and D. P. DeWitt, *Introduction to Heat Transfer*, 3rd ed., Wiley, New York (1996).

Kudva, R. A., H. Keskkula, and D. R. Paul, "Morphology and Mechanical Properties of Compatibilized Nylon 6/Polyethylene Blends," *Polymer*, **40**, 6003 (1999).

Lai, E., and D. W. Yu, "Modeling of the Plasticating Process in a Single-Screw Extruder: A Fast Track Approach," *Poly. Eng. Sci.*, **40**, 1074 (2000).

Levitt, L., C. W. Macosko, and S. D. Pearson, "Influence of Normal Stress Difference on Polymer Drop Deformation," *Poly. Eng. Sci.*, **36**, 1647 (1996).

Li, H. X., G. H. Hu, and J. A. Sousa, "The Early Stage of the Morphology Development of Immiscible Polymer Blends During Melt Blending: Compatibilized vs. Uncompatibilized Blends," *J. Poly. Sci.: Part B: Poly. Phys.*, **37**, 3368 (1999).

Lindt, J. T., and A. K. Ghosh, "Fluid Mechanics of the Formation of Polymer Blends 1: Formation of Lamellar Structures," *Poly. Eng. Sci.*, **32**, 1802 (1992).

Majumdar, B., H. Keskkula, and D. R. Paul, "Mechanical Properties and Morphology of Nylon-6/Acrylonitrile-Butadiene-Styrene Blends Compatibilized with Imidized Acrylic Polymers," *Polymer*, **35**, 5453 (1994).

Oshinski, A. J., H. Keskkula, and D. R. Paul, "The Role of Matrix Molecular Weight in Rubber Toughened Nylon 6 Blends 1: Morphology," *Polymer*, **37**, 4891 (1996).

Potente, H., and U. Melisch, "Theoretical and Experimental Investigations of the Melting of Pellets in Co-Rotating Twin-Screw Extruders," *Intern. Poly. Process.*, **11**, 101 (1996).

Potente, H., and M. Bastian, "Polymer Blends in Co-Rotating Twin-Screw Extruders," *Intern. Poly. Process.*, **16**, 14 (2001).

Potente, H., M. Bastian, K. Bergemann, M. Senge, G. Scheel, and T. Winkelmann, "Morphology of Polymer Blends in the Melting Section of Co-Rotating Twin Screw Extruders," *Poly. Eng. Sci.*, **41**, 222 (2001).

Qian, B. N., and C. G. Gogos, "The Importance of Plastic Energy Dissipation (PED) to the Heating and Melting of Polymer Particulates in Intermeshing Co-Rotating Twin-Screw Extruders," *Adv. Poly. Tech.*, **19**, 287 (2000).

Rao, B. K., "Heat Transfer to Non-Newtonian Flows Over a Cylinder in Cross Flow," *Int. J. Heat Fluid Flow*, **21**, 693 (2000).

Sastrohartono, T., Y. Jaluria, and M. V. Karwe, "Numerical Simulation of Fluid Flow and Heat Transfer in Twin-Screw Extruders for Non-Newtonian Materials," *Poly. Eng. Sci.*, **35**, 1213 (1995).

Scott, C. E., and C. W. Macosko, "Model Experiments Concerning Morphology Development During the Initial Stages of Polymer Blending," *Poly. Bull.*, **26**, 341 (1991).

Scott, C. E., and C. W. Macosko, "Morphology Development During the Initial Stages of Polymer-Polymer Blending," *Polymer*, **36**, 461 (1995).

Subramanian, P. M., "Permeability Barriers by Controlled Morphology of Polymer Blends," *Poly. Eng. Sci.*, **25**, 483 (1985).

Sundararaj, U., C. W. Macosko, R. J. Rolando, and H. T. Chan, "Morphology Development in Polymer Blends," *Poly. Eng. Sci.*, **32**, 1814 (1992).

Sundararaj, U., and C. W. Macosko, "Drop Breakup and Coalescence in Polymer Blends: The Effects of Concentration and Compatibilization," *Macromolecules*, **28**, 2647 (1995).

Sundararaj, U., Y. Dori, and C. W. Macosko, "Sheet Formation in Immiscible Polymer Blends," *Polymer*, **36**, 1957 (1995).

Sundararaj, U., "Effect of Processing Parameters on Phase Inversion During Polymer Blending," *Rev. Makromol. Chem. Makromol. Symp.*, **112**, 85 (1996).

Tenge, S., and D. Mewes, "Experimental Investigation of the Energy Balance for the Metering Zone of a Twin Screw Extruder," *Poly. Eng. Sci.*, **40**, 277 (2000).

Utracki, L. A., and Z. H. Shi, "Development of Polymer Blend Morphology During Compounding in a Twin-Screw Extruder 1: Droplet Dispersion and Coalescence—A Review," *Poly. Eng. Sci.*, **32**, 1824 (1992).

Van Krevelen, D. W., and P. J. Hoftyzer, "Newtonian Shear Viscosity of Polymeric Melts," *Angew. Makromol. Chem.*, **52**, 101 (1976).

Willis, J. M., V. Caldas, and B. D. Favis, "Processing Morphology Relationships of Compatibilized Polyolefin Polyamide Blends: 2. The Emulsifying Effect of an Ionomer Compatibilizer as a Function of Blend Composition and Viscosity Ratio," *J. Mater. Sci.*, **26**, 4742 (1991).

Wu, S., "Phase Structure and Adhesion in Polymer Blends—A Criterion for Rubber Toughening," *Polymer*, **26**, 1855 (1985).

Manuscript received July 1, 2002, revision received Dec. 9, 2002, and final revision received Feb. 18, 2003.